INTERNATIONAL JOURNAL FOR NUMERICAL METHODS IN FLUIDS
Int. J. Numer. Meth. Fluids 2007; **55**:1059–1089
Published online 8 May 2007 in Wiley InterScience (www.interscience.wiley.com). DOI: 10.1002/fld.1514

Kinetic meshless method for compressible flows‡

C. Praveen[1,*,†] and S. M. Deshpande[2]

[1]*ARDB CFD Center, Department of Aerospace Engineering, Indian Institute of Science, Bangalore 560012, India*
[2]*Engineering Mechanics Unit, Jawaharlal Nehru Center for Advanced Scientific Research, Jakkur, Bangalore 560064, India*

SUMMARY

We present a grid-free or meshless approximation called the kinetic meshless method (KMM), for the numerical solution of hyperbolic conservation laws that can be obtained by taking moments of a Boltzmann-type transport equation. The meshless formulation requires the domain discretization to have very little topological information; a distribution of points in the domain together with local connectivity information is sufficient. For each node, the connectivity consists of a set of nearby nodes which are used to evaluate the spatial derivatives appearing in the conservation law. The derivatives are obtained using a modified form of the least-squares approximation. The method is applied to the Euler equations for inviscid flow and results are presented for some 2-D problems. The ability of the new scheme to accurately compute inviscid flows is clearly demonstrated, including good shock capturing ability. Comparisons with other grid-free methods are made showing some advantages of the current approach. Copyright © 2007 John Wiley & Sons, Ltd.

Received 9 May 2006; Revised 20 December 2006; Accepted 29 December 2006

KEY WORDS: meshless method; kinetic scheme; least squares; Euler equations

1. INTRODUCTION

The numerical solution of partial differential equations requires the generation of a grid or mesh in the computational domain. Mesh generation technology has seen rapid advances in the last two to three decades. The development of multi-block and unstructured meshing techniques now allows investigation of 3-D problems involving complex geometries. In spite of these advances, mesh generation is still the most difficult and time-consuming part of the simulation procedure. This difficulty is compounded when the geometry is complex with multiple bodies,

*Correspondence to: C. Praveen, Project OPALE, INRIA, 2004 Route des Lucioles, 06902 Sophia Antipolis, France.
†E-mail: praveen@bluehome.net
‡This work was conducted while the first author was a research scholar in the Department of Aerospace Engineering at the Indian Institute of Science, Bangalore.

small gaps, deforming boundaries and bodies in relative motion. For a realistic 3-D configuration, grid generation can take several hundred man-hours of work. The quality of the numerical solution depends on the quality of the mesh which puts increased burden on the task of grid generation.

Meshless methods are expected to overcome many of these difficulties associated with grid generation. The basic idea in meshless methods is to remove the requirement of a grid or mesh; instead a distribution of points in the computational domain is used for the numerical solution of the partial differential equations. The points need not be arranged in any regular pattern and can even be randomly distributed. The only geometrical information required on the point distribution is the local *connectivity*, i.e. for each point we need to know the set of neighbouring points which will form the stencil for the numerical approximation. We use the words *connectivity* and *stencil* to mean the same thing. A stencil is generally associated with a fixed topology but in the case of meshless methods it is arbitrary. The generation of a point distribution is expected to be much easier than generating a grid. There are two approaches to generating a point distribution. The first and easiest way is to use existing grid generation tools to construct a grid and then take the vertices of the grid as the points [1, 2]. The second way of obtaining a point distribution is to directly generate the points without generating a grid. Löhner [3] has developed an advancing front point generation technique which is an order of magnitude faster than unstructured grid generation. Recently, Varma *et al*. [4] are developing point distributions using quadtree/octree approach which is expected to be highly automatic and capable of handling complex configurations. Using meshless methods, we are also freed from the problem of having to deal with small cut cells and associated issues [5].

The most commonly used discretization procedure in meshless methods is the *least-squares approximation*. The basic idea of this approach is to assume a certain functional form of the unknown function and fit the parameters using a least-squares minimization. The functional form can be obtained in several ways, the most common being a truncated Taylor's series. The use of least-squares gives the meshless character to the scheme. Ghosh and Deshpande [6] used the least-squares technique to develop the least-squares kinetic upwind method (LSKUM), a kinetic upwind meshless approximation for Euler equations governing inviscid compressible flows which are hyperbolic. Batina [7] proposed a meshless method based on artificial dissipation and solved Euler equations over full aircraft. Morinishi [8] and Löhner *et al*. [9] have developed an upwind-type method for hyperbolic equations and solved 2-D and 3-D problems. However, in both the methods the upwind directions are not determined from physical considerations but by the geometry of point distributions. Balakrishnan and Praveen [10, 11] and Sridar and Balakrishnan [12] have developed a class of upwind meshless schemes for conservation laws which were inspired by flux-differencing ideas. These schemes have been applied to many test cases involving 2-D inviscid and viscous flows. All the above methods can be regarded as generalized finite difference schemes since they contain the usual finite differences as special cases.

The outline of the paper is as follows. The basic idea of LSKUM is briefly discussed followed by kinetic meshless method (KMM). The dual least squares (DLS) is introduced and is used to derive the KMM. Some theoretical advantages of using a kinetic formulation are then discussed. The KMM is extended to higher-order accuracy using a reconstruction approach. Boundary conditions are introduced and a numerical order of accuracy study is performed on a model scalar conservation law. The rotational invariance property of KMM is proved. Finally, the results of numerical computations are presented for a large number of test cases.

DOI: 10.1002/fld

2. LEAST-SQUARES KINETIC UPWIND METHOD

The LSKUM is a kinetic meshless method which is based on the idea of kinetic schemes [13, 14]. An upwind meshless discretization of the Boltzmann equation [15] leads to an upwind scheme at the Euler level after taking moments [15, 16] in the velocity space. The upwind discretization is constructed at the kinetic level where the molecular velocities define the upwind directions. One-sided (also called *split* or *half*) stencils which are chosen based on the sign of the molecular velocity are used to discretize the spatial derivatives arising in the Boltzmann equation. The use of split stencils gives the upwind character to LSKUM.

The Euler equations governing inviscid compressible flows can be written in the conservation form as follows:

$$\frac{\partial U}{\partial t}+\frac{\partial}{\partial x}GX+\frac{\partial}{\partial y}GY=0 \tag{1}$$

where $U=[\rho, \rho u_x, \rho u_y, E]^\top$ is the vector of conserved variables and (GX, GY) are the Cartesian components of the flux vector,

$$GX=[\rho u_x,\ p+\rho u_x^2,\ \rho u_x u_y,\ (E+p)u_x]^\top,\quad GY=[\rho u_y,\ \rho u_x u_y,\ p+\rho u_y^2,\ (E+p)u_y]^\top \tag{2}$$

In the above equations ρ is the density, $\mathbf{u}=(u_x, u_y)$ is the fluid velocity, p is the pressure and E is the energy per unit volume. For an ideal gas, we have $p=\rho RT$ where R is the gas constant and T is the absolute temperature. The energy density is given by $E=p/(\gamma-1)+\rho|\mathbf{u}|^2/2$. In the present work the numerical computations are performed with $R=287\,\mathrm{Nm/kg}$ and $\gamma=1.4$, which is the ratio of specific heats.

The Euler equations can be obtained from the Boltzmann equation without collision term

$$\frac{\partial F}{\partial t}+v_x\frac{\partial F}{\partial x}+v_y\frac{\partial F}{\partial y}=0 \tag{3}$$

by taking moments in the velocity space defined by

$$\langle\cdot\rangle=\int\!\!\int\!\!\int \Psi(v_x, v_y, I)(\cdot)\,\mathrm{d}v_x\,\mathrm{d}v_y\,\mathrm{d}I \tag{4}$$

where F is the Maxwellian velocity distribution function [15], (v_x, v_y) are the Cartesian components of molecular velocity, I is an additional variable corresponding to non-translational degrees of freedom, and $\Psi=[1, v_x, v_y, I+(v_x^2+v_y^2)/2]^\top$ are the collisional invariants. In order to introduce upwinding the *full* stencil C_o at any point P_o is *split* into four parts as indicated in Table I. The Boltzmann equation is then discretized as

$$\frac{\mathrm{d}F_o}{\mathrm{d}t}+\frac{v_x+|v_x|}{2}\left(\frac{\partial F}{\partial x}\right)_{C_1}+\frac{v_x-|v_x|}{2}\left(\frac{\partial F}{\partial x}\right)_{C_2}+\frac{v_y+|v_y|}{2}\left(\frac{\partial F}{\partial y}\right)_{C_3}+\frac{v_y-|v_y|}{2}\left(\frac{\partial F}{\partial y}\right)_{C_4}=0$$

Table I. Split stencils for 2-D LSKUM.

x-split	$C_1=\{P_j\in C_o \mid x_j\leqslant x_o\}$	$C_2=\{P_j\in C_o \mid x_j\geqslant x_o\}$
y-split	$C_3=\{P_j\in C_o \mid y_j\leqslant y_o\}$	$C_4=\{P_j\in C_o \mid y_j\geqslant y_o\}$

DOI: 10.1002/fld

and after taking moments we obtain

$$\frac{\mathrm{d}U_o}{\mathrm{d}t} + \left(\frac{\partial}{\partial x} GX^+\right)_{C_1} + \left(\frac{\partial}{\partial x} GX^-\right)_{C_2} + \left(\frac{\partial}{\partial y} GY^+\right)_{C_3} + \left(\frac{\partial}{\partial y} GY^-\right)_{C_4} = 0 \tag{5}$$

where $GX^{\pm}$, $GY^{\pm}$ are kinetic split fluxes [16]. In LSKUM, the derivatives are computed using a least-squares fit [6] on the corresponding stencil. LSKUM is extended to higher-order accuracy using entropy variables and defect correction; the resulting scheme is known as q-LSKUM [17] which also makes use of split stencils for flux derivatives as in Equation (5). The boundary conditions for LSKUM/q-LSKUM are also derived at the molecular level using the specular reflection model of kinetic theory [15], and make use of stencils which are split along the tangent to the boundary [6].

3. KINETIC MESHLESS METHOD

The stencil C_o used in q-LSKUM must contain sufficient points so that each of the four split stencils defined in Table I contains atleast three points (excluding P_o) so that the least-squares problem is over-determined. This might lead to an increase in the stencil size and loss of local nature of the stencil. For points near boundaries there may not be sufficient neighbours available in some of the split stencils. In such cases, we have to use the full stencil for the corresponding split flux derivatives. Moreover, the least-squares problem on each split stencil must be well conditioned and must give accurate estimates of derivatives [18]. The full stencil is usually well behaved in terms of these requirements [18]. Hence, it would be useful to develop a meshless scheme that does not require stencil sub-division and the KMM was developed with this criteria in mind.

In KMM, the approximation is performed with a single *full* stencil C_o and there is no need to split the stencil. Each stencil will in general have fewer number of points and a smaller support. q-LSKUM uses split stencils in order to satisfy the upwind principle. In KMM, upwinding is introduced with the help of a modified least-squares approximation called the *dual least-squares* (DLS) approximation. In DLS, we introduce *mid-point* states which are defined in an *upwind* manner leading to a stable discretization. The idea of mid-point states in a least-squares framework has also been used by Morinishi [8], Balakrishnan and Praveen [10, 11], Sridar and Balakrishnan [12], Löhner *et al*. [9] and Junk [19], at the macroscopic level while in the present work the kinetic approach is used to derive the scheme. We show that this kinetic approach has some advantages in terms of the size of the matrices involved and better conditioning of the least-squares problem.

3.1. Dual least-squares approximation

Let P_o be the point where we want to approximate the derivatives and select a connectivity C_o as shown in Figure 1. Assume that the value of F at the mid-point of the line $\overline{P_o P_j}$ is known and denote it as $F_{j/2}$. Using Taylor's formula we can write

$$F_{j/2} = F_o + \frac{1}{2}\Delta x_j \frac{\partial F}{\partial x} + \frac{1}{2}\Delta y_j \frac{\partial F}{\partial y} + O(h^2), \quad j = 1, \ldots, N$$

DOI: 10.1002/fld

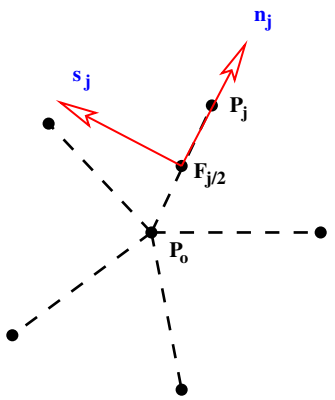

Figure 1. Definition of rotated coordinate frame for computation of mid-point fluxes.

where $\Delta x_j = x_j - x_o$, $\Delta y_j = y_j - y_o$, N is the number of points in the stencil of P_o, the derivatives are at node P_o and h is some characteristic point spacing. Neglecting the $O(h^2)$ terms we get the following system of equations:

$$F_{j/2} = F_o + \frac{1}{2}\Delta x_j \frac{\partial F}{\partial x} + \frac{1}{2}\Delta y_j \frac{\partial F}{\partial y}, \quad j = 1, \ldots, N \tag{6}$$

which is over-determined since $N > 2$. The two unknown derivatives are determined by solving a weighted minimization problem

$$\min \sum_j w_j [F_{j/2} - F_o - (\Delta x_j/2)\partial_x F - (\Delta y_j/2)\partial_y F]^2 \quad \text{wrt } \partial_x F,\ \partial_y F$$

where ∂_x, ∂_y denote partial differentiation with respect to x, y, respectively. This leads to a system of two coupled equations, called the *normal* equations,

$$\begin{bmatrix} \sum w_j \Delta x_j^2 & \sum w_j \Delta x_j \Delta y_j \\ \sum w_j \Delta x_j \Delta y_j & \sum w_j \Delta y_j^2 \end{bmatrix} \begin{bmatrix} \partial_x F \\ \partial_y F \end{bmatrix} = 2 \begin{bmatrix} \sum w_j (F_{j/2} - F_o) \Delta x_j \\ \sum w_j (F_{j/2} - F_o) \Delta y_j \end{bmatrix} \tag{7}$$

The solution of the above equations can be written in compact form as follows:

$$\left(\frac{\partial F}{\partial x}\right)_{C_o} = \sum_j a_j (F_{j/2} - F_o), \quad \left(\frac{\partial F}{\partial y}\right)_{C_o} = \sum_j b_j (F_{j/2} - F_o) \tag{8}$$

where the coefficients (a_j, b_j) are given by

$$a_j = 2\frac{(\sum w_k \Delta y_k^2) w_j \Delta x_j - (\sum w_k \Delta x_k \Delta y_k) w_j \Delta y_j}{D_o} \tag{9}$$

$$b_j = 2\frac{(\sum w_k \Delta x_k^2) w_j \Delta y_j - (\sum w_k \Delta x_k \Delta y_k) w_j \Delta x_j}{D_o} \tag{10}$$

DOI: 10.1002/fld

and

$$D_o = \sum w_j \Delta x_j^2 \sum w_j \Delta y_j^2 - (\sum w_j \Delta x_j \Delta y_j)^2 \tag{11}$$

is the determinant of the matrix in Equation (7). By Cauchy–Schwarz inequality, the determinant is always non-negative, $D_o \geqslant 0$, and is zero if and only if

$$\Delta y_j = \text{constant} \times \Delta x_j \quad \text{for all } j \in C_o$$

i.e. if all the points in C_o lie on a straight line passing through P_o. In this case, the derivatives cannot be determined since the least-squares problem is singular (degenerate case). The positive quantities w_j in the least-squares formulation are monotonically decreasing functions of distance between two points. In this work, we use inverse distance weights which are given by $w_j = (\Delta x_j^2 + \Delta y_j^2)^{-p/2}$ with $p \geqslant 0$.

Remark
There is a slightly different way of representing the solution of the least-squares approximation which is also useful for coding purposes. The set of weighted over-determined equations (6) can be written as

$$\sqrt{W} X \nabla F = \sqrt{W} \Delta F \tag{12}$$

where

$$\nabla F = \begin{bmatrix} \partial_x F \\ \partial_y F \end{bmatrix}, \quad X = \frac{1}{2} \begin{bmatrix} \Delta x_1 & \Delta y_1 \\ \Delta x_2 & \Delta y_2 \\ \vdots & \vdots \\ \Delta x_N & \Delta y_N \end{bmatrix}, \quad \Delta F = \begin{bmatrix} F_{1/2} - F_o \\ F_{2/2} - F_o \\ \vdots \\ F_{N/2} - F_o \end{bmatrix} \tag{13}$$

and

$$\sqrt{W} = \text{diag}[\sqrt{w_1} \ \sqrt{w_2} \ \ldots \ \sqrt{w_N}] \tag{14}$$

Equation (12) is over-determined since $N > 2$ and we solve it using a least-squares fit

$$\text{minimize } (X \nabla F - \Delta F)^\top W (X \nabla F - \Delta F) \quad \text{wrt } \nabla F \tag{15}$$

where ∇F is the gradient vector of F. The solution of this minimization problem gives

$$\nabla F = (X^\top W X)^{-1} X^\top W \Delta F =: M \Delta F \tag{16}$$

The matrix M is of size $2 \times N$ and its entries contain the coefficients (a, b),

$$M = (X^\top W X)^{-1} X^\top W = \begin{bmatrix} a_1 & a_2 & \ldots & a_N \\ b_1 & b_2 & \ldots & b_N \end{bmatrix} \tag{17}$$

DOI: 10.1002/fld

3.2. Derivation of KMM

The KMM is built on the DLS approximation together with upwind-biased specification of mid-point distribution at the kinetic level. Substituting the DLS approximation (8) into the Boltzmann equation (3) we obtain

$$\frac{\mathrm{d}F_o}{\mathrm{d}t} + v_x \sum a_j (F_{j/2} - F_o) + v_y \sum b_j (F_{j/2} - F_o) = 0 \tag{18}$$

The mid-point velocity distributions $F_{j/2}$ are as yet unspecified. The simplest approximation is to use averaging, $F_{j/2} = (F_o + F_j)/2$, but this leads to a central difference-type discretization which is unstable for hyperbolic equations. To obtain a stable discretization an upwind bias has to be introduced into the numerical scheme. In kinetic schemes, the upwind directions are determined by the molecular velocities and hence we take the following approximation:

$$F_{j/2} = \begin{cases} F_o & \text{if } \mathbf{v} \cdot \hat{n}_j \geqslant 0 \\ F_j & \text{if } \mathbf{v} \cdot \hat{n}_j \leqslant 0 \end{cases} \tag{19}$$

where $\hat{n}_j$ is a unit vector directed from P_o to P_j as shown in Figure 1. Using Equation (19) in (18) and taking moments we obtain the semi-discrete update equation for the conserved variables

$$\frac{\mathrm{d}U_o}{\mathrm{d}t} + \sum [a_j (GX_{j/2} - GX_o) + b_j (GY_{j/2} - GY_o)] = 0 \tag{20}$$

where $GX_{j/2}, GY_{j/2}$ are the mid-point fluxes given by

$$\begin{aligned} GX_{j/2} &= \langle v_x F_{j/2} \rangle = R_j^{-1} [A_j \cos\theta_j - B_j \sin\theta_j] \\ GY_{j/2} &= \langle v_y F_{j/2} \rangle = R_j^{-1} [A_j \sin\theta_j + B_j \cos\theta_j] \end{aligned} \tag{21}$$

where θ_j is the angle made by $\hat{n}_j$ with the positive x-axis, and

$$A_j = GX^+(R_j U_o) + GX^-(R_j U_j), \quad B_j = GY^{x+}(R_j U_o) + GY^{x-}(R_j U_j) \tag{22}$$

and R_j is the rotation matrix given by

$$R_j = R(\theta_j) = \begin{bmatrix} 1 & 0 & 0 & 0 \\ 0 & \cos\theta_j & \sin\theta_j & 0 \\ 0 & -\sin\theta_j & \cos\theta_j & 0 \\ 0 & 0 & 0 & 1 \end{bmatrix} \tag{23}$$

The expressions for the split fluxes are given in the Appendix. Equation (20) is an ordinary differential equation in time; in the present work we integrate these equations using a three-stage Runge–Kutta scheme [18].

Remark

If the point distribution is obtained from a Cartesian mesh and using a standard four-point stencil, the above scheme reduces to finite volume method with kinetic split fluxes [16].

Remark

The extension of the above scheme to 3-D is straightforward and is given in [18].

DOI: 10.1002/fld

3.3. Kinetic versus macroscopic formulation

A meshless scheme can be formulated directly at the macroscopic, i.e. the Euler level, in contrast to the Boltzmann level. Examples of such meshless schemes can be found in [8, 9, 12]. Let us look at a macroscopic scheme [12] which also uses DLS approximation but at the macroscopic level so that we deal with flux vectors. Let $\mathbf{G} = (GX, GY)$ denote the flux vector. Using the same notations and definitions of KMM, we can approximate the directed flux $\mathbf{G}_{j/2} \cdot \hat{n}_j$ at the mid-point of $\overline{P_o P_j}$ as

$$\begin{aligned}\mathbf{G}_{j/2} \cdot \hat{n}_j &= \mathbf{G}_o \cdot \hat{n}_j + \frac{1}{2}\Delta x_j \frac{\partial}{\partial x}(\mathbf{G}_o \cdot \hat{n}_j) + \frac{1}{2}\Delta y_j \frac{\partial}{\partial y}(\mathbf{G}_o \cdot \hat{n}_j) + O(h^2) \\ &= \mathbf{G}_o \cdot \hat{n}_j + \frac{1}{2}\frac{\Delta x_j^2}{\Delta r_j} \underbrace{\frac{\partial}{\partial x} GX_o}_{1} + \frac{1}{2}\frac{\Delta y_j^2}{\Delta r_j} \underbrace{\frac{\partial}{\partial y} GY_o}_{2} \\ &\quad + \frac{1}{2}\frac{\Delta x_j \Delta y_j}{\Delta r_j} \underbrace{\left(\frac{\partial}{\partial x} GY_o + \frac{\partial}{\partial y} GX_o\right)}_{3} + O(h^2)\end{aligned}$$

Neglecting the $O(h^2)$ terms, there are three unknowns in the above equation and we can pose the following minimization problem with respect to the unknowns:

$$\begin{aligned}\min \sum_j \Delta r_j^2 \Bigg[&\mathbf{G}_{j/2} \cdot \hat{n}_j - \mathbf{G}_o \cdot \hat{n}_j - \frac{1}{2}\frac{\Delta x_j^2}{\Delta r_j}\frac{\partial}{\partial x} GX_o - \frac{1}{2}\frac{\Delta y_j^2}{\Delta r_j}\frac{\partial}{\partial y} GY_o \\ &- \frac{1}{2}\frac{\Delta x_j \Delta y_j}{\Delta r_j}\left(\frac{\partial}{\partial x} GY_o + \frac{\partial}{\partial y} GX_o\right)\Bigg]^2\end{aligned}$$

This leads to a system of three coupled equations which can be written in matrix notation as $A_e X_e = b_e$ where

$$A_e = \begin{bmatrix} \sum \Delta x_j^4 & \sum \Delta x_j^2 \Delta y_j^2 & \sum \Delta x_j^3 \Delta y_j \\ \sum \Delta x_j^2 \Delta y_j^2 & \sum \Delta y_j^4 & \sum \Delta x_j \Delta y_j^3 \\ \sum \Delta x_j^3 \Delta y_j & \sum \Delta x_j \Delta y_j^3 & \sum \Delta x_j^2 \Delta y_j^2 \end{bmatrix}, \quad X_e = \begin{bmatrix} \partial_x GX_o \\ \partial_y GY_o \\ \partial_y GX_o + \partial_x GY_o \end{bmatrix} \tag{24}$$

Note that only the first two elements of X_e, $\partial_x GX$ and $\partial_y GY$, are required for the numerical solution. The 2-D kinetic formulation (see Equation (7)) gives a 2×2 matrix given by[§]

$$A_k = \begin{bmatrix} \sum \Delta x_j^2 & \sum \Delta x_j \Delta y_j \\ \sum \Delta x_j \Delta y_j & \sum \Delta y_j^2 \end{bmatrix} \tag{25}$$

[§]The weights are ignored since they do not change the conclusions of this section.

DOI: 10.1002/fld

In 3-D macroscopic formulation we obtain a set of six equations for six unknowns out of which only three are required for the numerical solution; the corresponding 6×6 matrix which is symmetric is given by [20]

$$\begin{bmatrix} \sum \Delta x_j^4 & \sum \Delta x_j^2 \Delta y_j^2 & \sum \Delta x_j^2 \Delta z_j^2 & \sum \Delta x_j^3 \Delta y_j & \sum \Delta x_j^2 \Delta y_j \Delta z_j & \sum \Delta x_j^3 \Delta z_j \\ . & \sum \Delta y_j^4 & \sum \Delta y_j^2 \Delta z_j^2 & \sum \Delta x_j \Delta y_j^3 & \sum \Delta y_j^3 \Delta z_j & \sum \Delta x_j \Delta y_j^2 \Delta z_j \\ . & . & \sum \Delta z_j^4 & \sum \Delta x_j \Delta y_j \Delta z_j^2 & \sum \Delta y_j \Delta z_j^3 & \sum \Delta z_j^3 \Delta x_j \\ . & . & . & \sum \Delta x_j^2 \Delta y_j^2 & \sum \Delta x_j \Delta y_j^2 \Delta z_j & \sum \Delta x_j^2 \Delta y_j \Delta z_j \\ . & . & . & . & \sum \Delta y_j^2 \Delta z_j^2 & \sum \Delta x_j \Delta y_j \Delta z_j^2 \\ . & . & . & . & . & \sum \Delta x_j^2 \Delta z_j^2 \end{bmatrix}$$

On the other hand, the corresponding matrix for 3-D KMM is a 3×3 matrix given by

$$\begin{bmatrix} \sum \Delta x_j^2 & \sum \Delta x_j \Delta y_j & \sum \Delta x_j \Delta z_j \\ \sum \Delta x_j \Delta y_j & \sum \Delta y_j^2 & \sum \Delta y_j \Delta z_j \\ \sum \Delta x_j \Delta z_j & \sum \Delta y_j \Delta z_j & \sum \Delta z_j^2 \end{bmatrix}$$

We can make the following observations:

- Macroscopic formulation leads to matrices with larger dimensions (3×3 in 2-D and 6×6 in 3-D) compared to kinetic formulation (2×2 in 2-D and 3×3 in 3-D).
- The matrix elements in the macroscopic formulation are of order h^4 in contrast to kinetic formulation where the elements are of order h^2.
- Due to the above reasons the chances of ill-conditioning are more in the case of macroscopic formulation. This is indeed the case as shown in Section 4.9.
- The above differences will magnify when we go to higher-order formulation since the size of the matrix increases.
- There is a nice geometrical interpretation of solvability of the least-squares problem in the case of kinetic formulation (not all points should lie on a straight line/plane in 2-D/3-D) while no such characterization seems to be available in the case of macroscopic formulation.

The ill-conditioning of the matrix arising in the macroscopic formulation can be seen clearly when we apply it to a Cartesian point distribution. Taking a standard four-point stencil the matrix of the macroscopic formulation becomes

$$\text{diag}[2(h/2)^4, 2(h/2)^4, 0]$$

which is singular. On the other hand as mentioned before, KMM reduces to finite volume method on this standard Cartesian stencil. The fact that we are dealing with a single scalar function (velocity distribution function) in kinetic schemes as opposed to a flux vector leads to the above

DOI: 10.1002/fld

difficulties. We thus see an advantage in using a kinetic least-squares formulation as opposed to a least-squares formulation at the macroscopic level.

3.4. Higher-order scheme

The scheme defined by (19)–(21) has zeroth-order consistency in general, i.e. it is exact for a constant function. On a Cartesian point distribution on which KMM reduces to finite volume method, it has linear consistency also. On general point distributions, linear/first-order consistency is obtained by using the reconstruction approach similar to the finite volume methods. Let V be a complete set of macroscopic variables which uniquely determines the distribution function. In the present work the set of macroscopic variables for reconstruction is taken to be the primitive variables, $V = [\rho, \mathbf{u}, p]^\top$. Define the *left* and *right* states at the mid-point by linear interpolation

$$V_{j/2}^{+} = V_o + \tfrac{1}{2}\Delta\mathbf{r}_j \cdot \nabla V_o, \quad V_{j/2}^{-} = V_j - \tfrac{1}{2}\Delta\mathbf{r}_j \cdot \nabla V_j \tag{26}$$

The mid-point distribution function is now defined using the interpolated values

$$F_{j/2} = \begin{cases} F(V_{j/2}^{+}) & \text{if } \mathbf{v}\cdot\hat{n}_j \geqslant 0 \\ F(V_{j/2}^{-}) & \text{if } \mathbf{v}\cdot\hat{n}_j \leqslant 0 \end{cases} \tag{27}$$

Using this approximation in (18) and taking moments we obtain (20) but now the mid-point fluxes $GX_{j/2}$, $GY_{j/2}$ are evaluated with $V_{j/2}^{+}$, $V_{j/2}^{-}$ instead of V_o, V_j, respectively. The gradients of V are obtained using the coefficients (a_j, b_j), for example

$$\nabla V_o = \frac{1}{2}\sum (a_j, b_j)(V_j - V_o)$$

where the factor '$\frac{1}{2}$' is necessary because we are using the nodal values of V and not the mid-point values. The same coefficients $\{(a_j, b_j)\}$ are thus used for both the flux derivatives and for derivatives required in the reconstruction step. Scheme (20), (21), (27) has linear consistency on general point distributions. In Section 3.6 we perform numerical study of accuracy for a scalar conservation law which indicates second-order accuracy even on random point distributions. If the solution is discontinuous the numerical results will exhibit spurious oscillations due to loss of monotonicity. In this case, the gradients used in the reconstruction step must be limited in order to obtain wiggle-free solutions [18].

3.5. Boundary condition

For inviscid flows the velocity normal to a solid wall is zero if the wall is stationary and is equal to the normal velocity of the wall if the wall is moving

$$\mathbf{u}_{\text{fluid}} \cdot \hat{n} = \mathbf{u}_{\text{wall}} \cdot \hat{n}$$

In KMM we apply the interior scheme on the wall also and once all the variables are updated the wall normal velocity is reset to satisfy the wall boundary condition. For a stationary wall, if $\mathbf{u}'$ is

DOI: 10.1002/fld

the velocity obtained after updating by KMM, then the corrected velocity is given by

$$\mathbf{u} = \mathbf{u}' - (\mathbf{u}' \cdot \hat{n})\hat{n}$$

Since KMM is rotationally invariant it is not even necessary to rotate the coordinate frame for a wall point and the update is performed in the global coordinate frame. For lifting flows in subsonic and transonic conditions, the point vortex model [21] together with the assumption of constant entropy and enthalpy is used.

On the other hand, in q-LSKUM we have to rotate the coordinate system to the tangent–normal frame and make use of stencils split along the tangent [6]. In KMM we use a single stencil for boundary points also. The boundary conditions are thus inherent to each scheme and cannot be used interchangeably without violating the basic nature of each scheme.

3.6. Numerical order of accuracy

To investigate the numerical order of accuracy of KMM, we have applied it to the following scalar conservation law

$$\frac{\partial \rho}{\partial t} + \frac{\partial}{\partial x}(\rho u_x) + \frac{\partial}{\partial y}(\rho u_y) = 0, \quad t > 0, \quad (x, y) \in (0, 1) \times (0, 1) \tag{28}$$

where $\mathbf{u} = (u_x, u_y) = (y, -x)$. This equation can be obtained by taking moments (with $\Psi = 1$) of the Boltzmann equation (3) with a Maxwell-type distribution given by $F = (\rho\beta/\pi)\exp(-\beta|\mathbf{v} - \mathbf{u}|^2)$ for any $\beta > 0$. The initial conditions are

$$u(x, y, 0) = \begin{cases} u_o(y) & \text{on } x = 0 \\ 0 & \text{elsewhere} \end{cases}$$

where u_o is smooth and compactly supported in $[0, 1]$ so that the appropriate boundary conditions are $u(0, y, t) = u_o(y)$, $u(x, 1, t) = u(1, y, t) = 0$, $\forall t > 0$. The characteristics of Equation (28) are clockwise concentric circles centred at the origin so that the steady-state solution is $u_s(x, y) = u_o(\sqrt{x^2 + y^2})$. We use the following compactly supported data:

$$u_o(y) = \begin{cases} \sin^2(2\pi(y + 1/4)), & \frac{1}{4} < y < \frac{3}{4} \\ 0 & \text{elsewhere} \end{cases}$$

Equation (28) with $\beta = 0.1$ is solved on a sequence of uniform Cartesian and non-uniform/random point distributions which become successively finer. The non-uniform point distribution is obtained by randomly perturbing the uniform Cartesian point distribution. The perturbed coordinates $(\bar{x}, \bar{y})$ are given by $\bar{x} = x + 0.4\zeta\Delta x$ and $\bar{y} = y + 0.4\eta\Delta y$, where $\zeta, \eta \in [-1, 1]$ are random numbers. Figure 2 shows an example of uniform and non-uniform points used in this study. The solution contours on the finest uniform and random points is plotted in Figure 2(c) which shows that there is no visual difference in the two solutions. For each point distribution, the L_1, L_2 and L_∞ errors are calculated and these are plotted in Figure 3 against a point spacing size h which is defined as

$$h = \max_i \max_{j \in \mathscr{C}_i} |\mathbf{x}_j - \mathbf{x}_i|$$

DOI: 10.1002/fld

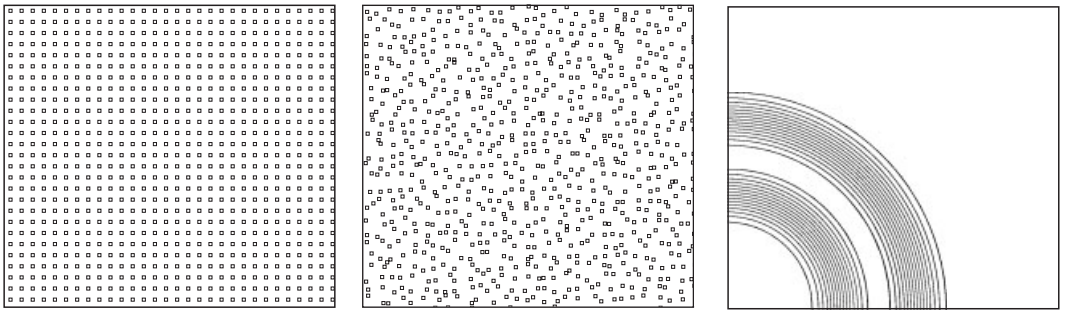

Figure 2. (a) Uniform; (b) random point distributions; and (c) solution for scalar test case.

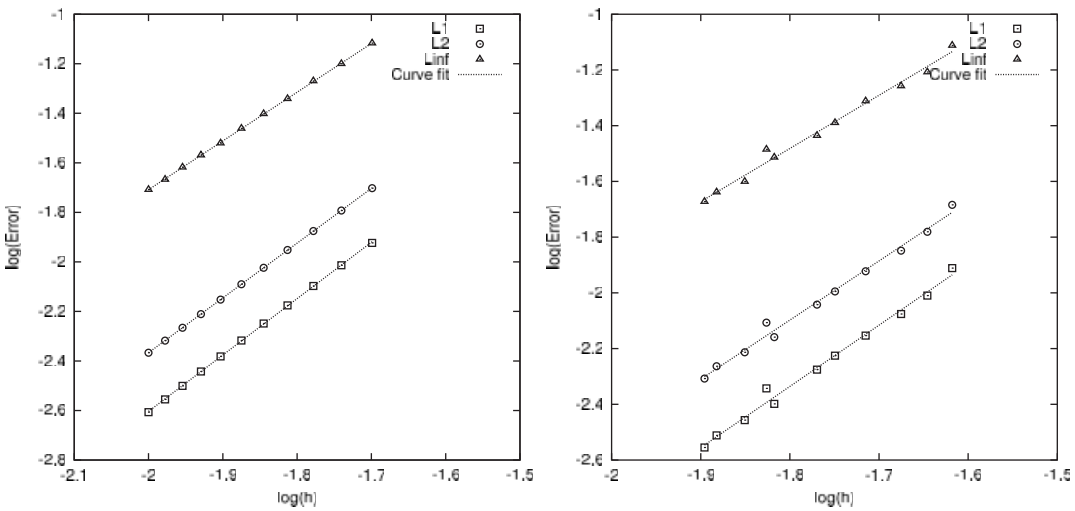

Figure 3. Error *versus* point spacing for uniform (left) and random (right) point distributions.

Table II. Computed order of accuracy on uniform and non-uniform point distributions.

Point distribution	L_1	L_2	L_∞
Uniform	2.27	2.21	1.97
Random	2.19	2.12	1.90

The slope of the best straight line fit for the error as a function of h in log–log scale gives the order of accuracy and these are listed in Table II. The best fit lines are also shown in Figure 3. These results show an effective second-order accuracy for the method.

DOI: 10.1002/fld

3.7. Rotational invariance property

The least-squares approximation can be performed in any local Cartesian coordinate system, unlike grid-based finite difference schemes in which the grid lines define the coordinate frame. Since the solution of the partial differential equations must be independent of the coordinate frame we expect the numerical scheme to be invariant to coordinate transformations. This invariance implies that the error in the numerical solution and the numerical dissipation do not depend on the coordinate frame which is an important property of genuinely multi-dimensional schemes. The least-squares approximation is invariant to coordinate translation since the difference of coordinates Δx_j, Δy_j are invariant. The other type of transformation is rotation of coordinate frame. Consider the term $\mathbf{v}\cdot\nabla F$ in the Boltzmann equation, which is a scalar and is invariant to rotational transformations. The DLS approximation is

$$\begin{aligned}\mathbf{v}\cdot\nabla F &= v_x\sum a_j(F_{j/2}-F_o)+v_y\sum b_j(F_{j/2}-F_o)\\ &= \sum(v_x a_j+v_y b_j)(F_{j/2}-F_o)\end{aligned}$$

Now F_o, $F_{j/2}$ are scalars and hence the DLS approximation is invariant if $(v_x a_j + v_y b_j)$ is a scalar. By the quotient rule of tensors [22] this is satisfied if (a_j, b_j) is a vector. If the coordinate frame is rotated by an angle θ then the coefficients in the new frame must be related to the (a_j, b_j) by

$$\begin{bmatrix}\bar{a}_j\\ \bar{b}_j\end{bmatrix} = S(\theta)\begin{bmatrix}a_j\\ b_j\end{bmatrix}, \quad S(\theta)=\begin{bmatrix}\cos\theta & \sin\theta\\ -\sin\theta & \cos\theta\end{bmatrix} \tag{29}$$

where S is the rotation matrix for a 2-D vector. In the new frame we have $\bar{X}=XS$, $\bar{W}=W$ so that the matrix of coefficients as given by Equation (17) in the new frame is given by

$$\bar{M}=(\bar{X}^\top\bar{W}\bar{X})^{-1}\bar{X}^\top\bar{W}=SM$$

which proves the desired result. This establishes the rotational invariance property of KMM at the Boltzmann level which will be preserved under moments. We next show the rotational invariance property directly at the Euler level by making use of some transformation properties of least-squares approximation.

Theorem 1
Let ϕ, $\mathbf{u}$ and σ be scalar, vector and second-order tensor field variables, respectively. Then,

1. $\Delta\mathbf{r}\cdot\nabla\phi$ is an invariant.
2. $\Delta\mathbf{r}\cdot\nabla\mathbf{u}$ is a vector.
3. $\nabla\cdot\mathbf{u}$ is an invariant.
4. $\nabla\cdot\sigma$ is a vector.

The least-squares estimates of the above quantities also have the same properties.

This theorem essentially says that the least-squares estimates of the derivatives of scalar, vector and tensor field variables share the transformation properties of the corresponding exact differential operator as shown in [18, 23].

DOI: 10.1002/fld

Theorem 2
The scheme defined by (20), (21), (26), (27) is rotationally invariant, i.e. if ρ^{n+1}, u_x^{n+1}, u_y^{n+1}, E^{n+1}, is the update in one coordinate frame and $\bar{\rho}^{n+1}$, $\bar{u}_x^{n+1}$, $\bar{u}_y^{n+1}$, $\bar{E}^{n+1}$, in any other frame, then they are related by,

$$\bar{\rho}^{n+1} = \rho^{n+1}, \quad \bar{E}^{n+1} = E^{n+1}, \quad \begin{bmatrix} \bar{u}_x^{n+1} \\ \bar{u}_y^{n+1} \end{bmatrix} = S \begin{bmatrix} u_x^{n+1} \\ u_y^{n+1} \end{bmatrix}$$

where S is the transformation matrix between the two frames.

Proof
See [18, 24]. □

4. NUMERICAL RESULTS

The KMM is applied to a number of 2-D test cases involving inviscid, compressible flows. The first set of test cases involve subsonic flows which do not contain any discontinuities and the second set of test cases involve discontinuities. The aim of solving these test cases is to demonstrate the good accuracy and robustness properties of KMM over a wide range of Mach numbers. For some of the test cases comparison with q-LSKUM results are also given which show the accuracy improvements obtained with KMM. Finally, the theoretical advantages of using kinetic-level formulation over a macroscopic formulation are confirmed by some numerical examples.

4.1. Selection of connectivity

The following test cases are solved on point distributions obtained from unstructured grids. While meshless methods do not require a grid, the aim of the present work is to demonstrate the capabilities of the new algorithm for solving a wide range of problems involving compressible flows. Hence, we use available grids to easily obtain point distributions and connectivity. The connectivity or the set of neighbouring nodes are obtained using the *edge connectivity* of the unstructured grid, i.e. by taking all points which are connected to a given point by edges as shown in Figure 4. This gives a small set of about four to six closest neighbours which is sufficient for the least-squares approximation in KMM. Once the connectivity is obtained for all points the grid structure

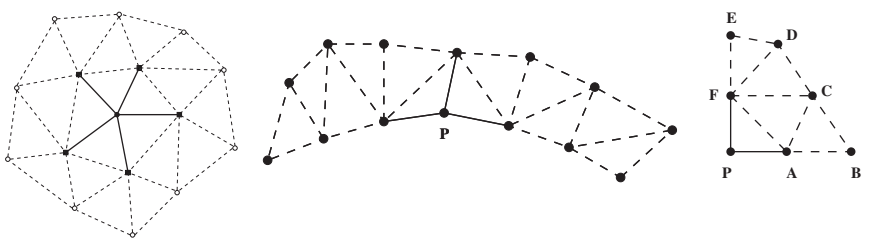

Figure 4. (Left) Connectivity selection for KMM; the solid lines give the edge neighbours (centre and right) connectivity for boundary points.

DOI: 10.1002/fld

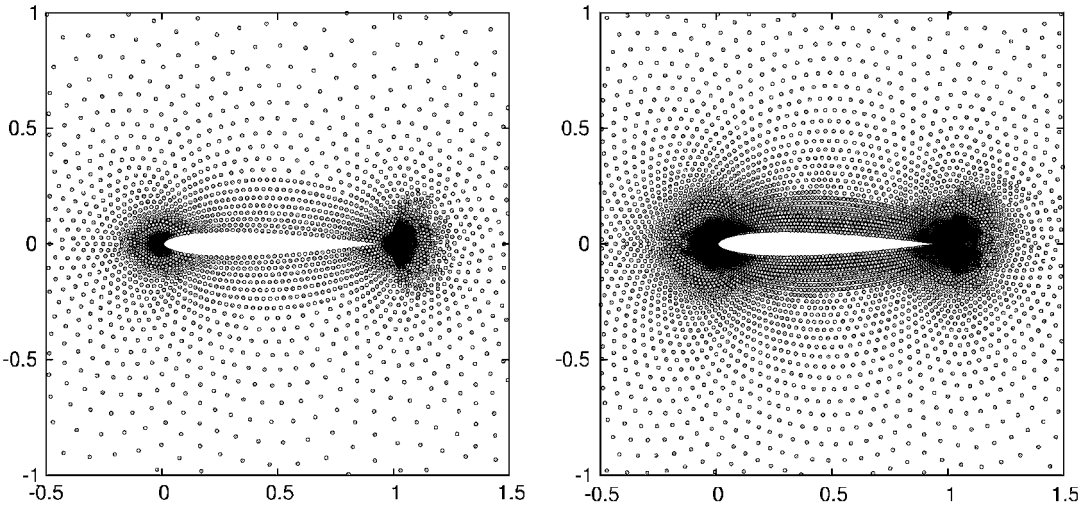

Figure 5. Point distributions for NACA-0012 airfoil: $G1$ (left) and $G2$ (right).

is not required by the flow solver. The geometric constraints on the connectivity for KMM are very minimal: (1) there must be atleast three points in the connectivity. This is required for the least-squares problem to be over-determined. (2) all the points in the connectivity must not lie on a straight line since this will make the least-squares problem indeterminate.

The least-squares problem must also be well conditioned and the full connectivity C_o at each point P_o must give accurate estimates of derivatives. Due to the absence of split stencils, we only need to check the quality of one stencil at each point. The condition numbers for all the un-adapted point distributions are less than 5 while for adapted points it is less than 50 which is acceptable. The connectivity given by edge neighbours usually has more than three points. For a boundary point P there might be only three edge neighbours as shown in Figure 4. This is still sufficient for KMM and there is no need to enhance the stencil. For a corner point P on the boundary as shown in Figure 4, there are only two edge neighbours in which case the connectivity is increased by adding secondary neighbours D and C. The neighbours B and E are not added since they lie on a line passing through points A and F, respectively, which are already in the connectivity. When there are more secondary neighbours, the required number of extra neighbours are added by selecting the closest points among them. For the two-point distributions for NACA-0012 airfoil shown in Figure 5 and labelled $G1$ and $G2$, the connectivity statistics are given in Table III. We note that almost 95% of the points have less than seven neighbours in the stencil.

The edge neighbours obtained from a triangulated grid lead to a small stencil with small spatial support. In practice, we may not have a triangulation but only a distribution of points. In such a case, a good approach is to first identify a local cloud of points using a search procedure like quadtree (octree in 3-D) and triangulate this local cloud. Note, however, that this triangulation is performed only to choose the stencil and so the quality of the triangulation is not very important.

If split stencils are used as in q-LSKUM then the primary (edge) neighbours may be insufficient in which case some secondary neighbours must be included in the connectivity. This can lead to an increase in the support of the connectivity. While the use of weights in the least-squares

DOI: 10.1002/fld

Table III. Connectivity statistics for NACA-0012 used in KMM and q-LSKUM.

Points	$G1$		$G2$	
N\scheme	KMM	q-LSKUM	KMM	q-LSKUM
3	0.11	—	0.10	—
4	3.69	—	2.83	—
5	6.13	—	3.93	—
6	84.40	0.27	89.61	0.13
7	5.56	0.18	3.42	0.17
8	0.09	30.38	0.11	27.32
9	—	63.24	—	68.16
10	—	5.88	—	4.21
11	—	0.05	—	0.01

Note: The table lists the percentage of points having a specified number (N) of neighbours.

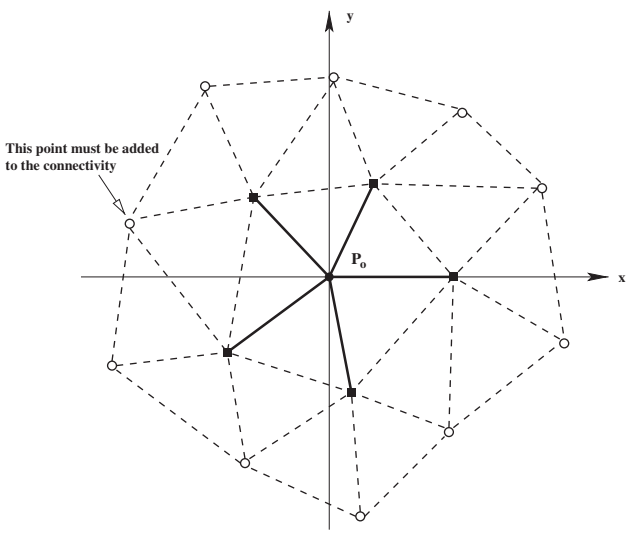

Figure 6. If split connectivity is used as in q-LSKUM then the primary neighbours are insufficient. An extra neighbour has to be added in the region $x<x_o$ as shown in this figure.

formula will reduce the effect of non-local data it cannot completely eliminate it since that would be equivalent to removing the neighbour. Figure 6 illustrates the enlargement of the connectivity in the case of split stencils since there are only two edge neighbours in the region $x<x_o$. Table III shows the connectivity statistics for q-LSKUM in which the edge connectivity has been enhanced so that there are atleast three points in each split stencil and we note a small increase in the connectivity size due to this requirement in q-LSKUM. If the points are obtained from a structured grid then the neighbours can be easily found using the (i, j)-indexing of the mesh. For KMM, it is enough to take a four-point connectivity consisting of $(i-1, j)$, $(i+1, j)$, $(i, j-1)$ and $(i, j+1)$.

DOI: 10.1002/fld

4.2. *Subsonic flow over Williams airfoil*

The Williams' airfoil is a two-element airfoil for which incompressible potential solution is available. The flow is computed at a low Mach number of 0.15 on a point distribution consisting of 6415 points. There are 234 points on the main airfoil and 117 points on the flap. Figure 7 shows a close-up view of the point distribution used in this computation. The connectivity statistics for KMM and q-LSKUM are shown in Table IV which reveals a small increase in connectivity size in the case of q-LSKUM.

The computed pressure coefficient on the airfoil and flap surface is shown in Figure 8 and are compared with exact analytical solution. This shows that KMM is much more accurate than q-LSKUM especially on the flap. Figure 9 shows the Mach number contours and also shows a zoomed up view of the Mach contours near the leading edge of the airfoil. The Mach contours in Figure 9 reveal distortion in the case of q-LSKUM and a numerical wake over the flap is also evident in Figure 9, both of which are due to excessive numerical entropy generation in the case of q-LSKUM while these are absent in the KMM results. The entropy should be constant throughout the domain since this is a low-speed flow and there are no shocks. A measure of entropy production is given by

$$S = \frac{p\rho^{-\gamma}}{(p\rho^{-\gamma})_\infty} - 1 \tag{30}$$

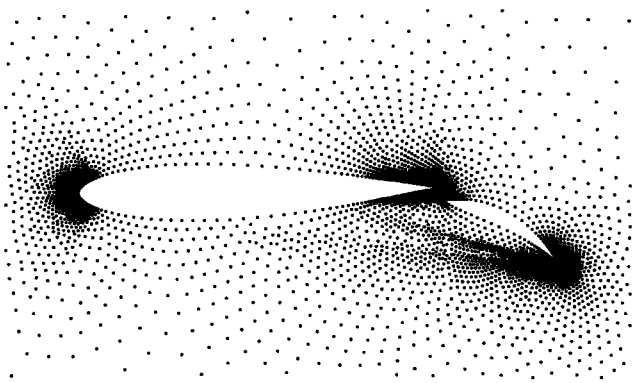

Figure 7. Point distribution for William's airfoil, close-up view.

Table IV. Connectivity statistics for Williams airfoil.

n	3	4	5	6	7	8	9
KMM	0.19	4.86	6.84	80.45	6.50	0.16	—
q-LSKUM	—	0.02	0.12	71.36	27.79	0.69	0.02

Note: The statistics for KMM are for edge connectivity while that for q-LSKUM is after enhancement such that there are three points in each split connectivity. q-LSKUM will not work on edge connectivity alone.

DOI: 10.1002/fld

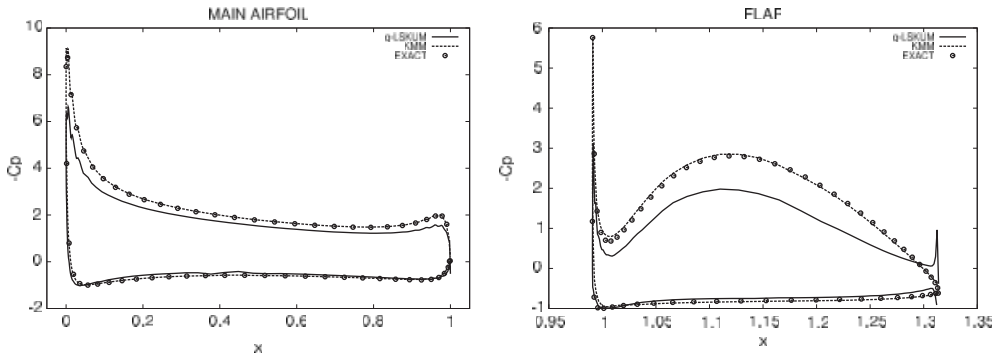

Figure 8. Comparison of pressure coefficients between KMM and q-LSKUM for flow over Williams airfoil.

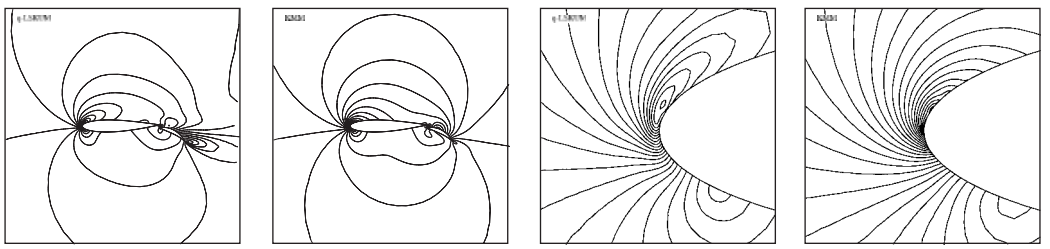

Figure 9. Williams airfoil: Mach contours using (a,c) q-LSKUM and (b,d) KMM.

In the case of KMM, the minimum and maximum entropies in the domain are $S_{\min} = -4.199 \times 10^{-4}$ and $S_{\max} = 7.246 \times 10^{-3}$. The lift and drag coefficients are 3.7608 and -0.0069 while the potential solution gives 3.736 and -0.0001, respectively.

In the case of q-LSKUM, the minimum and maximum entropies in the computational domain are $S_{\min} = -1.535 \times 10^{-3}$ and $S_{\max} = 1.031 \times 10^{-2}$, respectively, which is an order of magnitude larger than in the case of KMM. The lift and drag coefficients obtained with q-LSKUM are 3.093 and 0.0197, respectively. We see that KMM gives a better prediction of drag coefficient which is consistent with the fact that it produces less numerical entropy.

4.3. Subsonic flow over cylinder

Subsonic flow over a cylinder is computed at a free-stream Mach number of 0.38 using a total of 4111 points with 250 points on the cylinder. The connectivity statistics for KMM and q-LSKUM are shown in Table V. The Mach contours around the cylinder are shown in Figure 10(a) and (b). We see that the KMM solutions exhibit very good symmetry in the solution while the q-LSKUM results show loss of left-right symmetry. This is due to numerical entropy production which also leads to spurious separation and formation of an artificial wake in the case of q-LSKUM. In the case of KMM ($S_{\min} = -0.00138$, $S_{\max} = 0.000165$) we observe low levels of numerical entropy

DOI: 10.1002/fld

Table V. Connectivity statistics for 2-D cylinder.

n	4	5	6	7	8	9
KMM	6.67	5.50	83.12	4.72	—	—
q-LSKUM	—	0.19	82.56	16.78	0.44	0.02

Note: The statistics for KMM are for edge connectivity while that for q-LSKUM is after enhancement such that there are three points in each split connectivity.

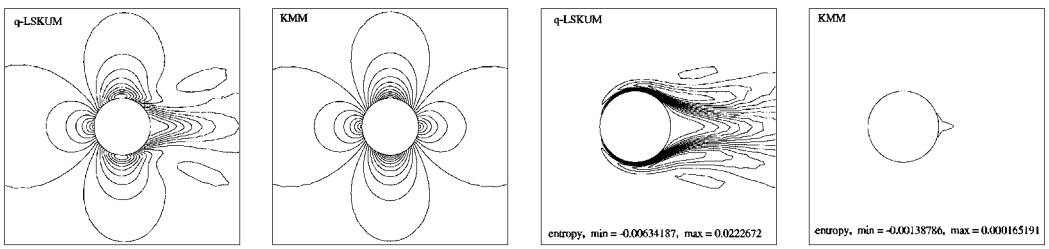

Figure 10. Flow over cylinder: (a, b) Mach number and (c, d) entropy contours.

production compared to q-LSKUM ($S_{\min} = -0.00634$, $S_{\max} = 0.022267$) as seen in Figure 10(c) and (d). The lift and drag coefficients obtained with KMM are 0.0006 and 0.0012 while those from q-LSKUM are 0.0237 and 0.0324, respectively. We note that KMM predicts values closer to zero indicating a more accurate solution.

4.4. Subsonic flow over Suddhoo–Hall airfoil

Suddhoo–Hall airfoil [25] is a four-element airfoil generated through conformal mapping techniques and hence the exact potential solution is known. The numerical solution is computed using KMM at a free-stream Mach number of 0.2 and zero angle of attack. The solution is computed on a point distribution consisting of 14 091 points. The circulation about the four elements is found to be 0.5387, 4.8095, 2.0925 and 0.7065 while the exact values are 0.5215, 4.7157, 2.0794 and 0.7216, respectively. The computed pressure coefficient on the airfoil surface is shown in Figure 11 together with the potential solution (symbols). It can be seen that the KMM solution compares very well with the exact solution indicating the good accuracy of the numerical scheme.

4.5. Subsonic flow over NACA-0012 airfoil

The NACA-0012 airfoil is a standard configuration for testing new algorithms. For this geometry, we use two points distributions labelled $G1$ and $G2$ as shown in Figure 5. In $G1$ there are 4385 points with 120 points on the airfoil while in $G2$ there are a total of 8912 points with 200 points on the airfoil. The subsonic flow past NACA-0012 airfoil at a free-stream Mach number of 0.63 and an angle of attack of 2° is computed on both the point distributions without using a limiter. The Mach number contours are shown in Figure 12 while the pressure coefficient on the airfoil surface is shown in Figure 14. The pressure coefficient in Figure 14 from q-LSKUM and KMM does not

DOI: 10.1002/fld

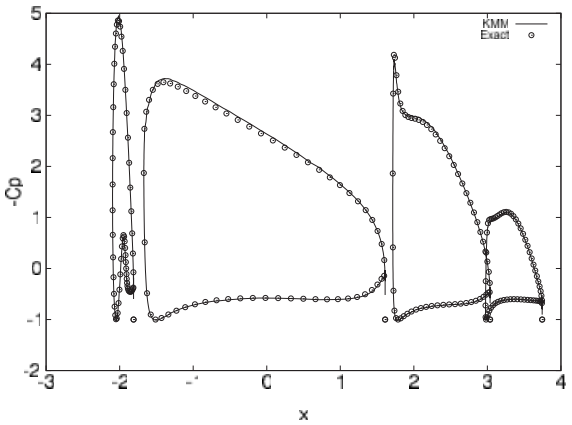

Figure 11. Pressure coefficient on the Suddhoo–Hall airfoil obtained using KMM (line) compared with potential solution (symbols).

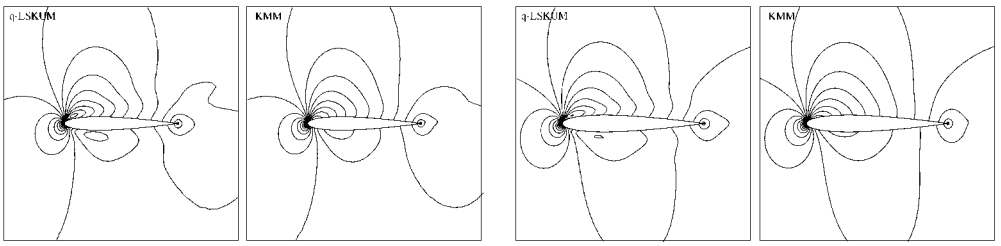

(a) (b)

Figure 12. Mach contours using q-LSKUM and KMM on two-point distributions: (a) $G1$, q-LSKUM and KMM and (b) $G2$, q-LSKUM and KMM.

show much difference but in the Mach contours we see a greater effect of numerical entropy in the case of q-LSKUM which leads to bending of Mach contours near the airfoil surface. This is also clearly seen in the entropy contours in Figure 13 which shows that q-LSKUM is generating higher numerical entropy. As the number of points increases from $G1$ to $G2$ the entropy generation in KMM is seen to reduce but q-LSKUM still generates a larger amount of spurious entropy. The lift and drag coefficients are given in Table VI where the GAMM results [26] are also indicated. The computed coefficients are seen to be within the range of GAMM results. The lift coefficient from both the schemes is seen to be close since the numerical dissipation does not strongly affect the pressure. The drag coefficient, which is ideally zero for this flow, is seen to be better predicted by KMM while q-LSKUM predicts slightly higher values of drag coefficient indicating larger amount of numerical dissipation.

4.6. Transonic flow over NACA-0012 airfoil

Transonic flow past NACA-0012 airfoil is computed at a free-stream Mach number of 0.85 and angle of attack of 1°. In this flow there is a shock on both the upper and lower surfaces of the airfoil

DOI: 10.1002/fld

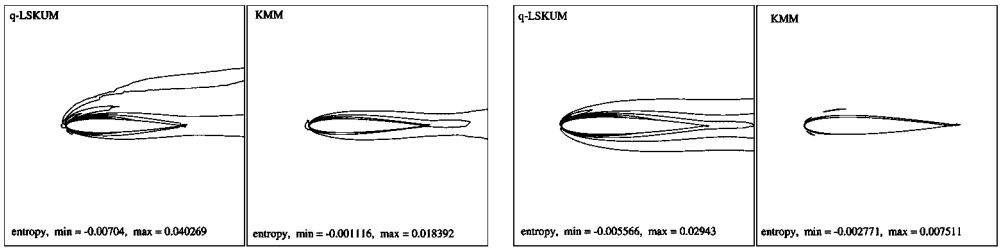

Figure 13. Entropy contours using q-LSKUM and KMM on two point distributions: (a) $G1$, q-LSKUM and KMM and (b) $G2$, q-LSKUM and KMM.

Table VI. Lift and drag coefficient for subsonic flow past NACA-0012.

	C_l		C_d	
Points	G_1	G_2	G_1	G_2
q-LSKUM	0.3358	0.3332	0.0029	0.0007
KMM	0.3263	0.3314	0.0016	0.0004
GAMM	0.329–0.336		0.003–0.07	

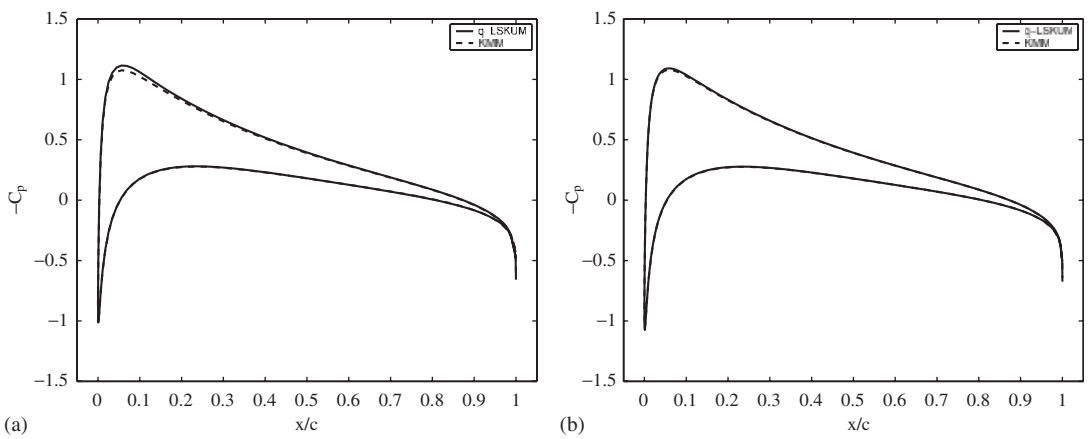

Figure 14. Comparison of pressure coefficient on (a) $G1$ and (b) $G2$ for subsonic flow over NACA-0012 airfoil.

as seen in the pressure coefficient in Figure 15 and Mach contours in Figure 16. These results also indicate good shock-capturing ability without any oscillations. On the finer-point distribution $G2$ almost a single-point shock is obtained. In Figure 15, the pressure coefficient on $G1$ and

DOI: 10.1002/fld

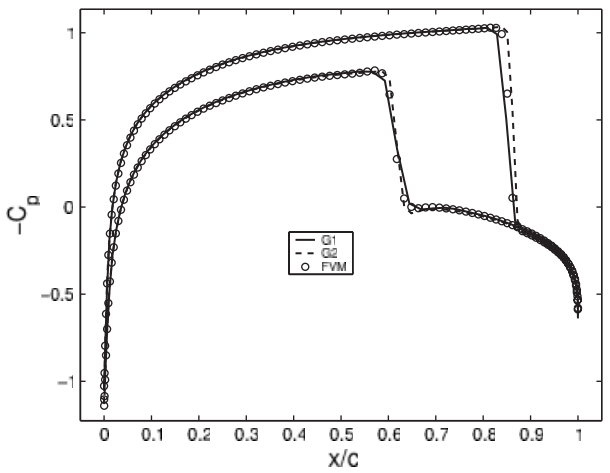

	C_l		C_d	
Points	G_1	G_2	G_1	G_2
q-LSKUM	0.3514	0.4162	0.0529	0.0588
KMM	0.3712	0.3888	0.0544	0.0567
AGARD	0.330-0.389		0.0464-0.0590	

Figure 15. Comparison of pressure coefficient (left) on $G1$, $G2$ using KMM with a finite volume solution on $G2$ for transonic over NACA-0012, and comparison of lift and drag coefficients from q-LSKUM and KMM (right).

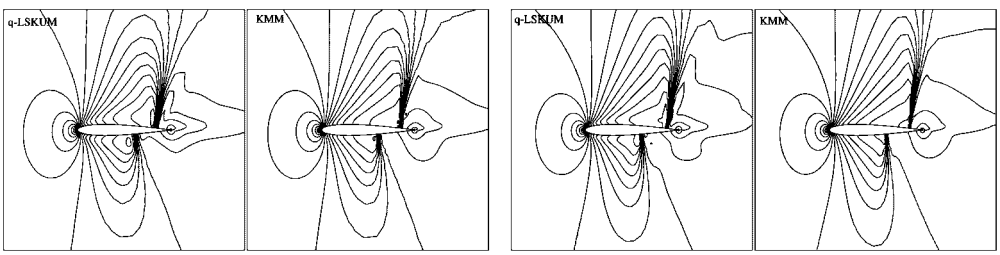

Figure 16. Mach contours from q-LSKUM and KMM on two-point distributions: (a) $G1$, q-LSKUM and KMM and (b) $G2$, q-LSKUM and KMM.

$G2$ are compared with a finite volume solution[¶] which indicates correct shock location has been obtained.

The transonic flow is also computed using q-LSKUM on the two-point distributions $G1$ and $G2$. As in the subsonic case the connectivity is enhanced in order to satisfy the minimum neighbours criteria. Figure 16 shows the comparison of the Mach contours with KMM. It can be seen that KMM gives slightly better resolution of the shocks. The entropy contours in Figure 17 show that KMM generates less spurious entropy in the leading edge portion of the airfoil while the maximum entropy level is similarly predicted by both the schemes. The spurious entropy is considerably reduced in the case of KMM on the finer-point distribution. The pressure coefficient is compared in Figure 18 which shows that both the schemes predict more or less same shock location. The lift

[¶]The finite volume solution is computed on $G2$ using KFVS fluxes [16].

DOI: 10.1002/fld

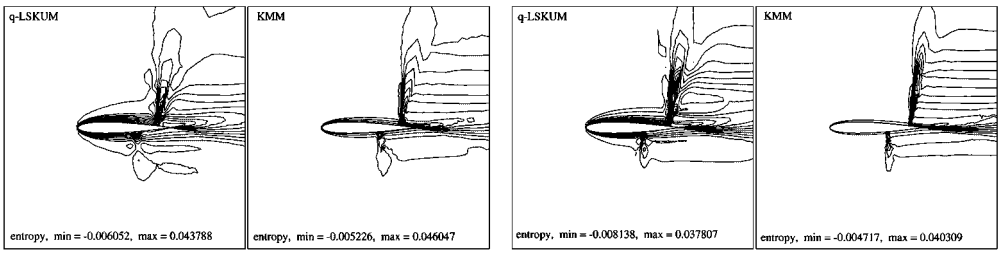

Figure 17. Entropy contours from q-LSKUM and KMM on two-point distributions: (a) $G1$, q-LSKUM and KMM and (b) $G2$, q-LSKUM and KMM.

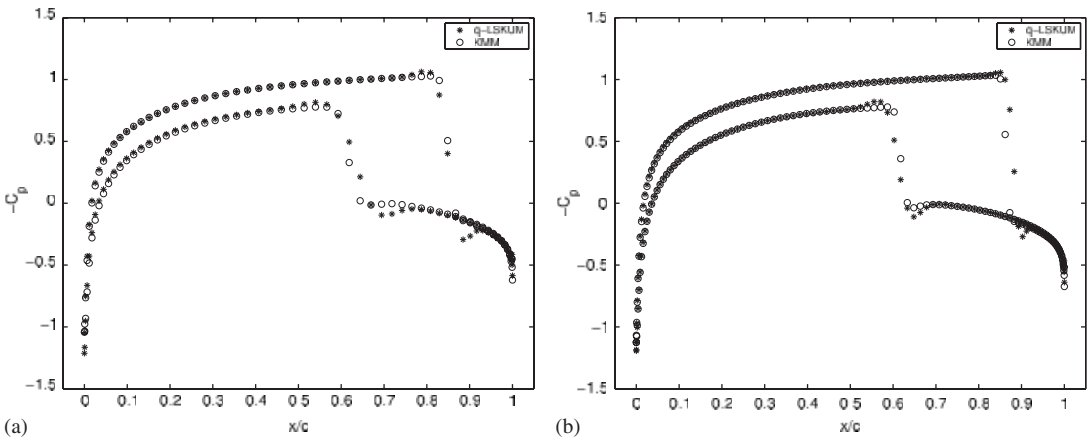

Figure 18. Pressure coefficient from q-LSKUM and KMM on two-point distributions: (a) $G1$ and (b) $G2$.

and drag coefficients are shown in Figure 15 which shows that the predicted values are in good agreement with the AGARD values [27].

The transonic flow is also computed on an adapted distribution of points[‖] shown in Figure 19(a). This point distribution is obtained after five levels of adaptation and contains a total of 3777 points. The Mach number contours are shown in Figure 19(b) which indicate that very sharp resolution of discontinuities is possible with KMM. The pressure coefficient on the airfoil surface is shown in Figure 19(c) where a finite volume solution is also shown (computed on $G2$). The KMM result is seen to resolve the shock without oscillations and the shock location agrees well with the finite volume solution.

[‖]The adaptation is performed using the unstructured grid and is not meshless in nature. An anisotropic adaptation software called BAMG [28, 29] was used which adapts based on all the four conserved variables.

DOI: 10.1002/fld

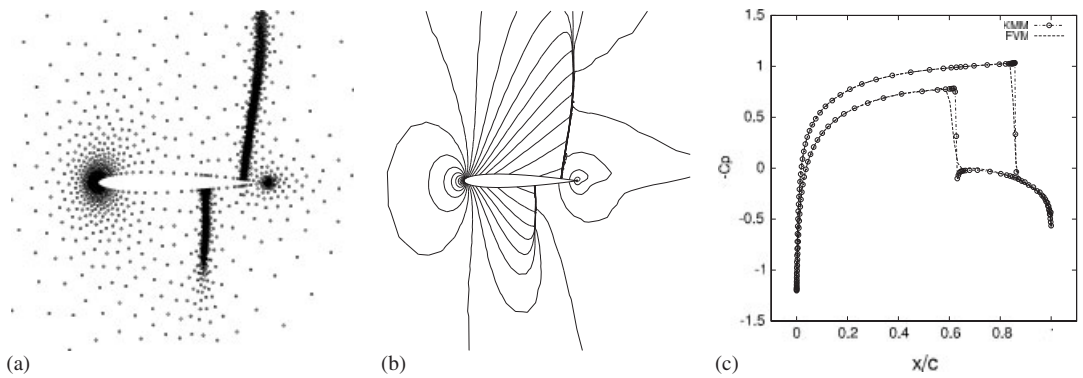

Figure 19. Transonic flow over NACA-0012 using KMM: (a) adapted point distribution; (b) Mach contours; and (c) pressure coefficient.

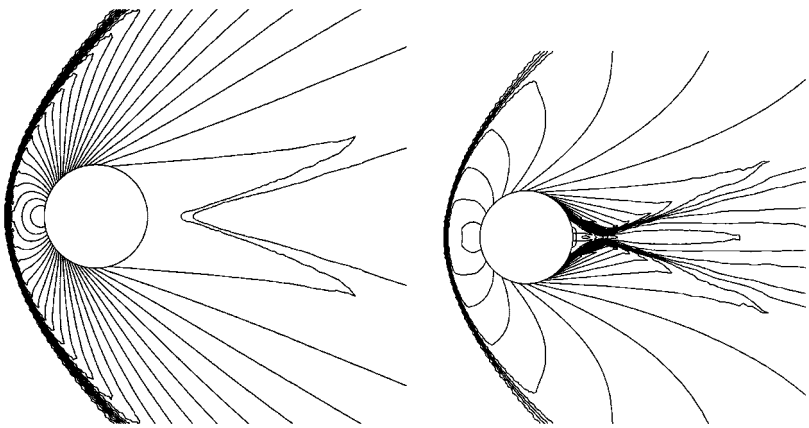

Figure 20. Pressure (left) and Mach number (right) contours for supersonic flow over 2-D cylinder obtained with KMM.

4.7. Supersonic flow over cylinder

Supersonic flow over a cylinder at $M_\infty = 3.0$ is computed on a distribution of 12 857 points. This flow has a bow shock ahead of the cylinder and a region of recirculating flow at the rear. Euler equations cannot be expected to give realistic solutions for such separated flows and we use this test to only demonstrate the robustness of the scheme. The gradients in the reconstruction are limited with min–max limiter and the CFL number of 0.1 is used. The computations ran without any problem of negative density/pressure which is quite common in this test case due to large expansion undergone by the flow in the rear portion of the cylinder. The pressure and Mach contours are shown in Figure 20; the Mach contours reveal a slip line on the leeward side of the cylinder. At the stagnation point behind the shock, the computed total pressure and total

DOI: 10.1002/fld

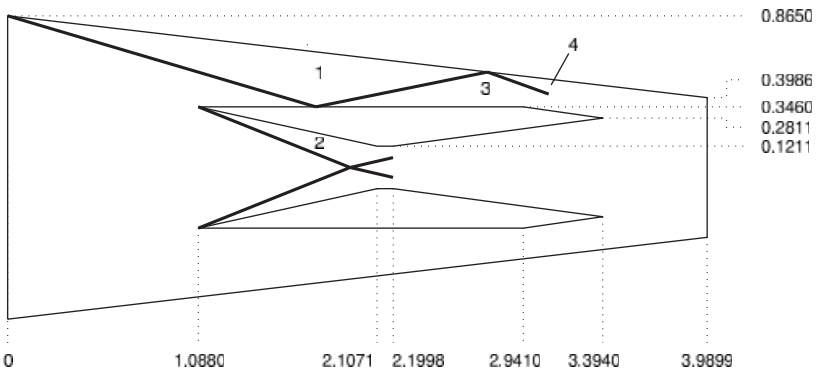

Figure 21. Geometry definition for scramjet intake.

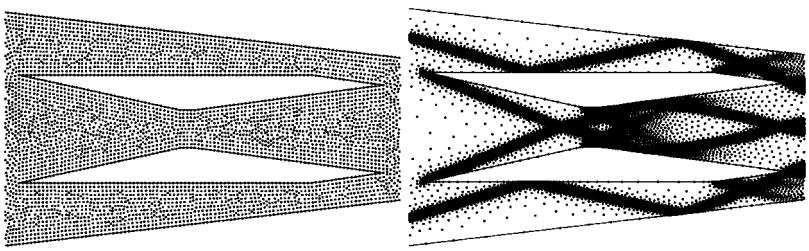

Figure 22. Initial (left) and adapted (right) point distribution for scramjet intake, zoomed up view.

temperature are 0.3234 and 1.0006, while the exact values are 0.3283 and 1.0000, respectively, which corresponds to an error of -1.5% and 0.06%. The lift and drag coefficients are found to be 0.00000 and 1.337, respectively.

4.8. Scramjet intake

This test case involves a 2-D model of a scramjet intake [30] whose geometry is shown in Figure 21. The flow involves a complex shock, expansion and contact discontinuity pattern and is a good test of accuracy and stability. The inlet conditions are $M = 5$, $\rho = 1$, $u = 1$ and $v = 0$. The computations are started on a point distribution of 8199 points shown on the left of Figure 22 and four levels of adaptation are performed leading to a point distribution with 34 997 points as shown on the right of Figure 22. The density contours on the initial and final point distributions are shown in Figure 23. The solution on the coarse point distribution shows all the gas dynamic features but they are poorly resolved. The finer-point distribution, however, shows very sharp resolution of discontinuities. The contours also show that the symmetry of the flow about the centre-line of the scramjet has been captured even though the point distribution is not exactly symmetric. The variation of Mach number and pressure on the centre-line is shown in Figure 24.

The flow field involves several shock reflections and the shock angles measured from the adapted solution are 16.44, 21.80, 18.12 and 20.32 while the exact values obtained from oblique shock

DOI: 10.1002/fld

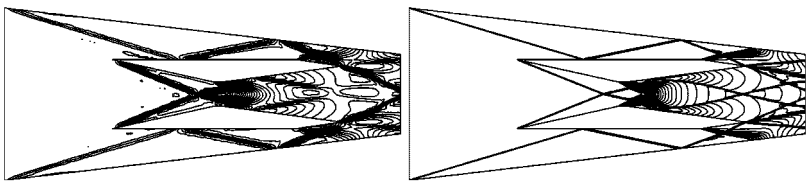

Figure 23. Density contours for a scramjet intake on initial (left) and adapted (right) point distributions.

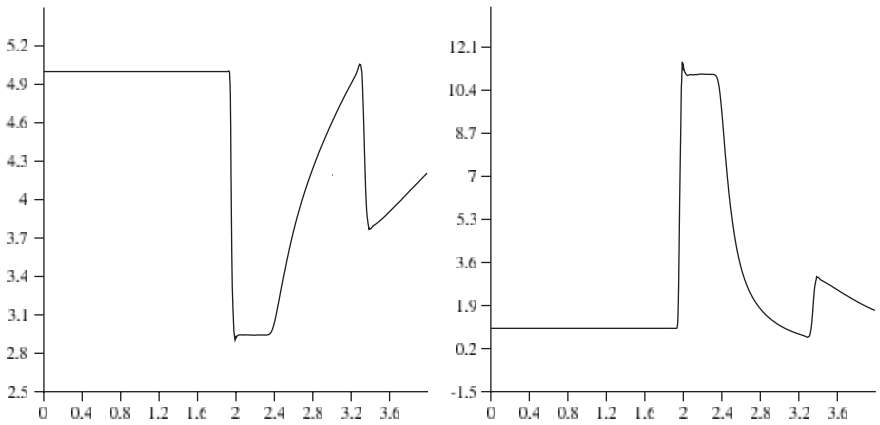

Figure 24. Mach number (left) and pressure (right) variation on the centre-line of scramjet intake obtained with adapted point distribution.

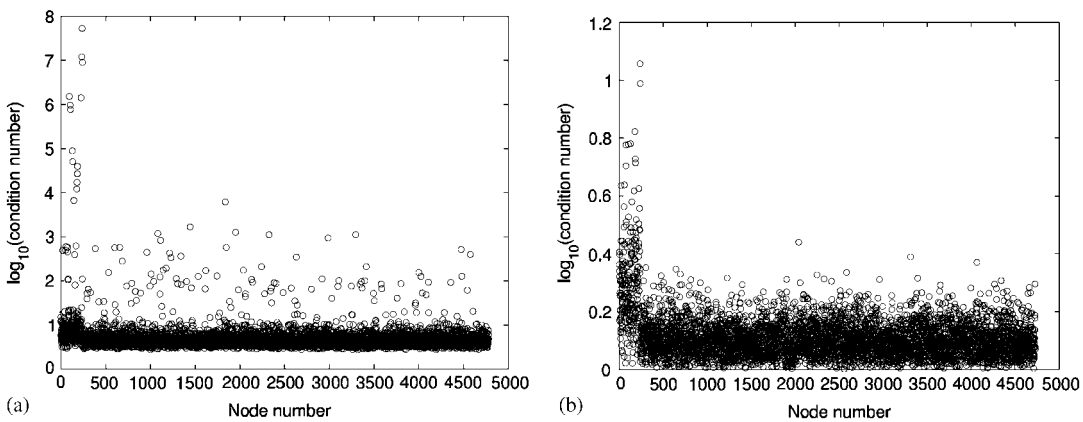

Figure 25. Condition numbers for: (a) macroscopic scheme and (b) kinetic scheme on point distribution obtained from unstructured grid with edge connectivity.

relations are 16.43, 21.72, 18.23 and 20.18, respectively. This test case clearly demonstrates that KMM is capable of resolving complex discontinuous flows very accurately provided the points are adapted based on the solution.

DOI: 10.1002/fld

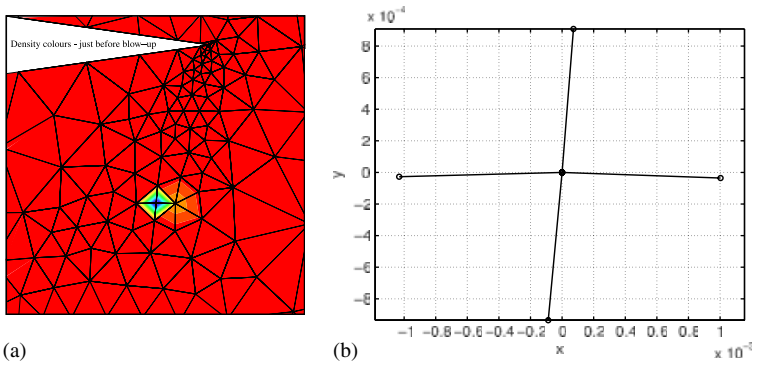

Figure 26. (a) Density contours just before blow-up with macroscopic scheme on edge connectivity (minimum connectivity size is 4). The singularity of matrix due to cross (Cartesian)-type connectivity is the cause of blow-up as seen in figure and (b) connectivity for point at which blow-up takes place.

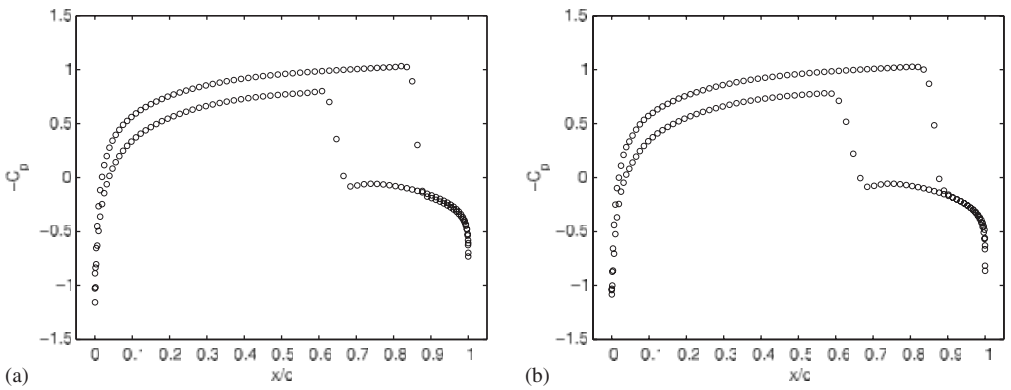

Figure 27. (a) Kinetic scheme using edge connectivity and (b) macroscopic scheme after enhancing connectivity to five neighbours.

4.9. Kinetic versus macroscopic scheme

Some theoretical properties of meshless methods based on kinetic and macroscopic formulations have been discussed in Section 3.3. Here, we present some numerical examples to show the relative advantage of kinetic formulation over a macroscopic formulation. We consider two-point distributions for NACA-0012 airfoil, the first one obtained from an unstructured grid and the second from a structured grid. For the unstructured point distribution we take the edge connectivity as described in Section 4.1 and compute the condition numbers of the matrices arising in the least-squares problem given by Equation (24) for the macroscopic formulation and by Equation (25) for the kinetic formulation. A scatter plot of the condition numbers is shown in Figure 25. We see that for the macroscopic formulation the condition numbers are generally very much higher, reaching even 10^7 while for the kinetic formulation it is within about 10. The macroscopic scheme is applied on these point distributions using KFVS [16] approximation for the flux $G_{j/2}\cdot\hat{n}_j$. The macroscopic scheme fails (negative density and pressure) on this edge connectivity at a point

DOI: 10.1002/fld

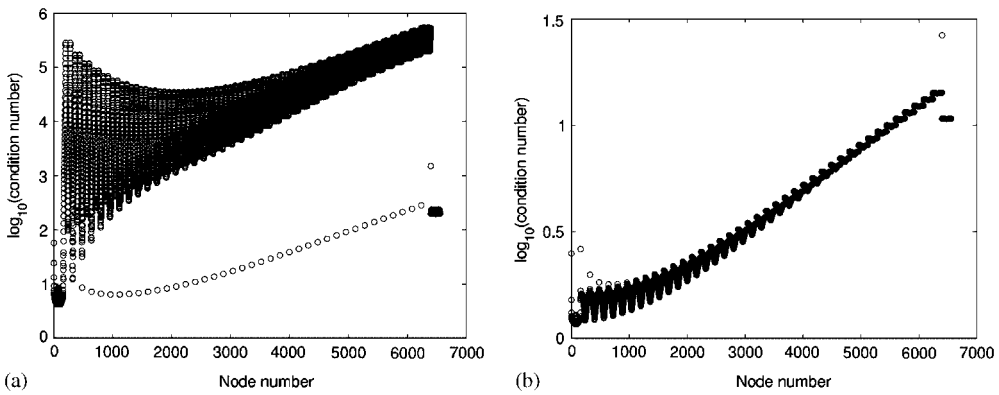

Figure 28. Condition numbers for: (a) macroscopic scheme and (b) kinetic scheme on points from structured grid. Most points have connectivity consisting of four neighbours.

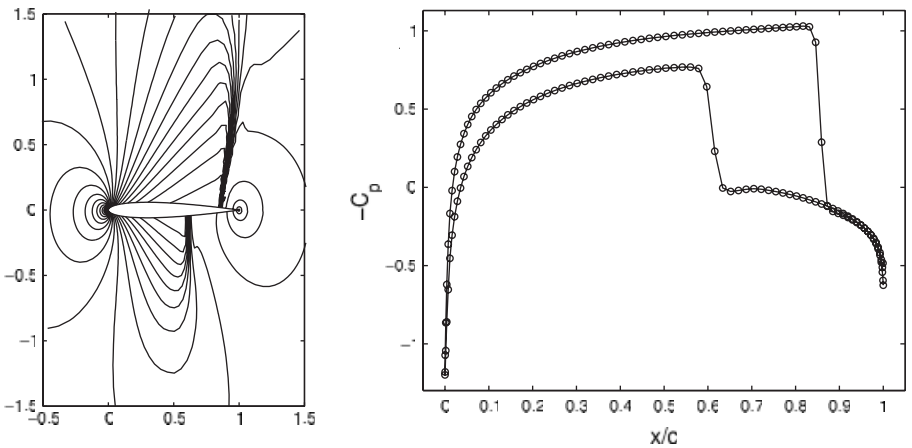

Figure 29. Pressure contours and pressure coefficient using KMM on a structured point distribution for NACA-0012. The connectivity is made up of standard four-point stencil.

shown in Figure 26(a). We note that the connectivity at this point is close to a standard Cartesian stencil as seen in Figure 26(b) which from Section 3.3 is known to be singular for the macroscopic scheme.

The kinetic scheme has no singularity problem on this connectivity with the condition numbers being closer to unity as seen in Figure 25(b) and converges to a good solution as seen in the pressure coefficient plot in Figure 27(a). For the macroscopic scheme the connectivity has to be modified so as to reduce the condition numbers. A crude way of achieving this is to add extra neighbours to all the points. For the present point distribution, the macroscopic scheme converges when we increase each connectivity to contain atleast five neighbours. Figure 27(b) shows the pressure coefficient of macroscopic scheme on the enhanced connectivity.

On the structured point distribution, the connectivity is selected using the (i, j)-indexing of the grid. For any node (i, j) the connectivity is taken to be standard four-point stencil consisting of

DOI: 10.1002/fld

$(i-1, j)$, $(i+1, j)$, $(i, j-1)$ and $(i, j+1)$. For a boundary point, the connectivity is $(i-1, j)$, $(i+1, j)$, $(i, j+1)$, $(i-1, j+1)$ and $(i+1, j+1)$. The condition numbers are plotted in Figure 28(a). We again see that the macroscopic formulation leads to high condition numbers ($\approx 10^5$) and in fact a large proportion of points are ill-conditioned. This is again due to the ill-conditioning we have discussed on the standard four-point Cartesian stencil. The kinetic formulation, however, leads to smaller condition numbers ($<10^{3/2}$) as seen in Figure 28(b). Due to this ill-conditioning the macroscopic scheme blows up on this connectivity, whereas the kinetic scheme has no problem in converging to a steady-state solution. The results of kinetic scheme shown in Figure 29 indicate that it gives good resolution of shocks. In order to run the macroscopic scheme on this point distribution the connectivity at a substantial number of points will have to be modified.

5. SUMMARY AND CONCLUSIONS

A new meshless method using kinetic theory and least squares is developed which unlike q-LSKUM does not require stencil sub-division. The upwind nature of the scheme is obtained by defining mid-point distribution functions based on the direction of molecular velocity. On a regular point distribution, this new scheme is shown to reduce to standard finite volume method based on KFVS. Some theoretical advantages of using a kinetic formulation for deriving the meshless scheme are shown in terms of smaller matrix size which can lead to better conditioning and hence fewer connectivity constraints. An order of accuracy study on a model scalar conservation law shows second-order accuracy. The scheme is also shown to be *rotationally invariant*, which is a property shared by all physical laws and is a pre-requisite for a genuinely multi-dimensional scheme.

The connectivity requirements of the solver are shown to be very minimal and the least-squares problem is seen to be well conditioned. In contrast, it is seen that q-LSKUM requires enhancement of connectivity in order to satisfy the over-determined condition and this is due to the stencil-splitting involved in q-LSKUM. The accuracy of KMM has been amply demonstrated on a wide variety of test cases and in conjunction with a limiter it is seen to be very robust. It is also shown to give more accurate solutions compared to q-LSKUM especially on the low subsonic test cases. With a suitable adaptation strategy very sharp resolution of discontinuities is possible with this meshless scheme. The advantage of using a kinetic formulation is demonstrated numerically by showing that the matrices are better conditioned than in a macroscopic formulation. This has many important practical consequences especially when we go to 3-D point distributions where good conditioning of the matrices involved is very essential for the stability of the numerical scheme.

APPENDIX A: KINETIC SPLIT FLUXES FOR 2-D KMM

$$GX^{\pm} = \begin{bmatrix} \rho(u_x A_x^{\pm} \pm B_x) \\ (p + \rho u_x^2) A_x^{\pm} \pm \rho u_x B_x \\ \rho(u_x A_x^{\pm} \pm B_x) u_y \\ (E+p) u_x A_x^{\pm} \pm (E + p/2) B_x \end{bmatrix}, \quad GY^{x\pm} = \begin{bmatrix} \rho u_y A_x^{\pm} \\ \rho(u_x A_x^{\pm} \pm B_x) u_y \\ (p + \rho u_y^2) A_x^{\pm} \\ (E+p) u_y A_x^{\pm} \pm \frac{1}{2} \rho u_x u_y B_x \end{bmatrix} \tag{A1}$$

DOI: 10.1002/fld

where

$$A_\alpha = \tfrac{1}{2}[1 + \mathrm{erf}(s_\alpha)], \quad B = \frac{\exp(-s_\alpha^2)}{2\sqrt{\pi\beta}}, \quad s_\alpha = \sqrt{\beta} u_\alpha \quad \text{for } \alpha = x, y$$

REFERENCES

1. Anandhanarayanan K, Nagarathinam M, Deshpande SM. Development and applications of a gridfree kinetic upwind solver to multibody configurations. *AIAA Paper No. 2005-4846*, June 2005.
2. Ramesh V, Deshpande SM. Euler computations on arbitrary grids using LSKUM. *First ICCFD*, Kyoto, Japan, July 2000.
3. Löhner R. An advancing front point generation technique. *Communications in Numerical Methods in Engineering* 1998; **14**:1097–1108.
4. Varma M, Rao SVR, Deshpande SM. Point generation using the quadtree data structure for meshless solvers. *FM Report No. 2003-FM-8*, Department of Aerospace Engineering, Indian Institute of Science, Bangalore, 2003.
5. Berger MJ, LeVeque RJ. Stable boundary conditions for Cartesian grid calculations. *ICASE Report No. 90-37*, NASA, 1990.
6. Ghosh AK, Deshpande SM. Least squares kinetic upwind method for inviscid compressible flows. *AIAA Paper 95-1735*, 1995.
7. Batina JT. A gridless Euler/Navier–Stokes solution algorithm for complex aircraft applications. *AIAA Paper 93-0333*, 1993.
8. Morinishi K. An implicit gridless type solver for the Navier–Stokes equations. *International Symposium on CFD*, Bremen, September 1999.
9. Löhner R, Sacco C, Onate E, Idelsohn. A finite point method for compressible flow. *International Journal for Numerical Methods in Engineering* 2002; **53**(8):1765–1779.
10. Balakrishnan N, Praveen C. A new upwind least squares finite difference scheme (LSFD-U) for Euler equations of gas dynamics. *Finite Volumes for Complex Applications*, vol. II. Hermes Science Publications: Paris, 1999; 331.
11. Praveen C, Balakrishnan N. New least squares based finite difference scheme for compressible flows. *Proceedings of the 8th Asian Congress of Fluid Mechanics*, Schenzen, China, 6–11 December 1999.
12. Sridar D, Balakrishnan N. An upwind finite difference scheme for meshless solvers. *Journal of Computational Physics* 2003; **189**:1–29.
13. Deshpande SM. Kinetic theory based new upwind methods for inviscid compressible flows. *AIAA Paper 86-0275*, 1986.
14. Deshpande SM. Kinetic flux splitting schemes. *Computational Fluid Dynamics Review*. Wiley: New York, 1995.
15. Chapman S, Cowling TG. *The Mathematical Theory of Non-Uniform Gases*. Cambridge University Press: Cambridge, 1952.
16. Mandal JC, Deshpande SM. Kinetic flux vector splitting for Euler equations. *Computers and Fluids* **23**(2):447–478.
17. Deshpande SM. Some recent developments in kinetic schemes based on least squares and entropy variables. *Conference on Solutions of PDE*, held in honour of Prof. Roe on the occasion of his 60th birthday, Arcachon, France, July 1998.
18. Praveen C. Development and application of kinetic meshless methods for Euler equations. *Ph.D. Thesis*, Department of Aerospace Engineering, Indian Institute of Science, Bangalore, July 2004 (Available from http://etd.ncsi.iisc.ernet.in/handle/2005/154/).
19. Junk M. Do finite volume methods really need a mesh? *International Workshop on Meshfree Methods for PDE*, Bonn, September 2001.
20. Deshpande SM, Praveen C. On meshless methods based on kinetic and macroscopic formulations. *FM Report*, *2003-FM-11*, Department of Aerospace Engineering, IISc, 2003.
21. Thomas JL, Salas MD. Far-field boundary condition for transonic lifting solutions to the Euler equations. *AIAA Paper No. 85-0020*, 1985.
22. Aris R. *Vectors*, *Tensors and the Basic Equations of Fluid Mechanics*. Dover: New York, 1989.
23. Praveen C. Some properties of the least squares formula. *FM Report*, *2001-FM-06*, Department of Aerospace Engineering, IISc, 2001 (Available from http://eprints.iisc.ernet.in/archive/00000138/).

DOI: 10.1002/fld

24. Praveen C, Deshpande SM. Rotationally invariant grid-less upwind method for Euler equations. *FM Report*, *2001-FM-08*, Department of Aerospace Engineering, IISc, 2001 (Available from http://eprints.iisc.ernet.in/archive/00000117/).
25. Suddhoo A, Hall M. Test cases for the plane potential flow past multi-element aerofoils. *Aeronautical Journal* 1985; Paper No. 1369.
26. GAMM Workshop on numerical solution of compressible Euler flows, 1986.
27. AGARD-AR-211. *Test Cases for Inviscid Flow Field Methods*.
28. *BAMG*, *Bi-dimensional Anisotropic Mesh Generation*. http://pauillac.inria.fr/cdrom/ftp/bamg
29. Castro Diaz MJ, Hecht F, Mohammadi B. New progress in anisotropic grid adaptation for inviscid and viscous flow simulations. *RR-2671*, INRIA, October 1995.
30. Kumar A. Numerical analysis of the scramjet-inlet flow field by using two-dimensional Navier–Stokes equations. *Technical Paper 1940*, NASA, December 1981.

DOI: 10.1002/fld